Exp Fluids (2009) 47:395–410
DOI 10.1007/s00348-009-0671-0

RESEARCH ARTICLE

Three-dimensional centrifugal instabilities development inside a parallelepipedic open cavity of various shape

Thierry M. Faure · Luc Pastur · François Lusseyran · Yann Fraigneau · Danièle Bisch

Received: 23 July 2008 / Revised: 27 April 2009 / Accepted: 29 April 2009 / Published online: 16 May 2009

Abstract This experimental study reports flow developments inside a parallelepipedic cavity of variable shape and dimensions. That flow is generated by the interaction between a laminar boundary layer and the cavity, which creates shear-layer oscillations. The aim is to understand the three-dimensional flow morphology varying the Reynolds number and the cavity shape. Flow visualizations are obtained in a plane situated inside the cavity in order to get the dynamical structures. Dimensional analysis of the cavity flow teaches that three dimensionless numbers are necessary for the flow reduction. This is confirmed by experimental results pointing thresholds of appearance of instabilities identified for some combinations of Reynolds number and geometric parameters. The key mechanisms for their existence are centrifugal effects induced by a vortex of spanwise axis with sufficient intensity, and viscous effects due to the wall confinement of the cavity. Their destruction is linked to flow transition to turbulence above a limiting convective velocity generated by the vortex of spanwise axis. These instabilities are generally present in a spanwise row of counter-rotating pairs of vortices, but for some cases, isolated pairs are also identified. Secondary modulations of primary instabilities are also present for particular parameters. Results permit to discriminate the relevant scales associated with the shear layer and the inner cavity flow.

T. M. Faure (✉) · L. Pastur · F. Lusseyran · Y. Fraigneau · D. Bisch
Laboratoire d'Informatique pour la Mécanique et les Sciences de l'Ingénieur, Unité Propre de Recherche 3251, Centre National de la Recherche Scientifique, B.P. 133, 91403 Orsay Cedex, France
e-mail: thierry.faure@limsi.fr

T. M. Faure
Université Pierre et Marie Curie, Paris 6, 4 Place Jussieu, 75252 Paris Cedex 05, France

L. Pastur
Université Paris-Sud, Paris 11, 91405 Orsay Cedex, France

List of symbols

A	Plate length upstream of the cavity
B	Plate length downstream of the cavity
D	Wind tunnel height
F	Span ratio
H	Cavity height
$\mathcal{H}$	Helicity
L	Cavity length
N	Number of pairs of spanwise vortices
R	Aspect ratio
Re	Reynolds number
S	Cavity span
t	Time
U_e	External velocity
U_c	Maximum advection velocity inside the cavity
$\vec{V}$	Velocity vector
W_s	Spanwise drift velocity
(x, y, z)	Cartesian coordinates
δ_2	Momentum thickness of the upstream boundary layer
λ	Spanwise wavelength of the instabilities
μ	Dynamics viscosity
ν	Kinematics viscosity
ρ	Density
$\vec{\omega}$	Vorticity

1 Introduction

The interaction between a boundary layer and a cavity results in a complex coupling of shear layer and recirculating flow (Pereira and Sousa 1995). That wall-bounded three-dimensional flow is the place for the development of primary instabilities whose dynamics is strongly led by the vortical flow motion inside the cavity. Such instabilities are found for different configurations.

The Görtler instability is a boundary layer instability induced by concave curvature. When the boundary layer is very small in comparison with the wall curvature radius, the centrifugal effects can be neglected in the basic state, which is considered as a quasi-parallel flow. However, centrifugal effects actually act in destabilizing the basic flow. The Görtler instability is the origin of transition to turbulence in bounded shear flow within low disturbance environment (Saric 1994). It is found from the range of low velocities (Cui 2004), to hypersonic flows (Aymer de la Chevalerie et al. 1997; Navarro-Martinez and Tutty 2005).

The Taylor-Couette instability is a centrifugal instability in a viscous flow confined by two rotating cylinders of radii R_1 and R_2. The basic state is the sum of a linear and a hyperbolic function of the radius. This instability has been widely studied for a narrow gap $d = R_2 - R_1$ with a stability transfer, above a critical threshold, between the basic state and stationary toroidal vortices. Similarly, Dean instability occurs for the same configuration with the presence of an azimuthal pressure gradient. Instability thresholds from the basic state to stationary vortex rings have also been established. An alternative approach of the shear-layer cavity flow has been conducted by its identification with the Taylor-Couette problem: the solid-body rotation of a central vortex is similar to the inner rotating cylinder and the cavity walls are the outer fixed cylinder (Brès and Colonius 2008). Then, it is possible to unify the previous types of instabilities into a single type coupling centrifugal effects and wall effects.

Flow dynamics studies have been achieved on lid-driven cavities for the same Reynolds number range as the present case: the difference is the absence of a developing unstable shear layer. Ghia et al. (1982) used a multi-grid method to simulate the flow inside a square lid-driven cavity, where a main vortex is developing along the whole length. Visualizations have been conducted by Koseff and Street (1984a, b, c) with dye emission, with tiny particle seeding by Migeon (2002) and Migeon et al. (2003) and comparisons with numerical simulations were carried out for the same measurements (Guermond et al. 2002). In these studies, a row of vortices was identified along the span.

This work considers centrifugal instabilities generated by the combination of wall curvature and a recirculating vortical flow inside a parallelepipedic cavity. A numerical simulation of the three-dimensional development of the cavity flow has been conducted for compressible flow conditions (Brès and Colonius 2008). The nature of the upstream boundary layer is important for the cavity flow developments (Chatellier et al. 2004; Chang et al. 2006). Visualizations in different planes have been reported previously (Faure et al. 2007) showing the main cavity flow morphology, for Reynolds numbers built on the cavity length, between 860 and 27,700. The driving mechanisms of the flow are the shear layer that is developing above the cavity, and at least one vortex of spanwise axis, developing inside the cavity.

The present study focuses on flow visualizations in a spanwise plane inside the cavity at very low Mach number, varying the length and the height of the shear-layer-driven cavity. The aim is to address the following issues:

- analyze whether the flow dynamics can be reduced to dimensionless numbers,
- give the flow morphology with cavity geometry and Reynolds number,
- track threshold parameters for which centrifugal vortices are present,
- provide features of centrifugal instability vortices.

2 Experimental setup and apparatus

The airflow is generated by a centrifugal fan placed upstream of a settling chamber (Fig. 1a). The seeding particle injection is achieved at the fan inlet. An axial duct

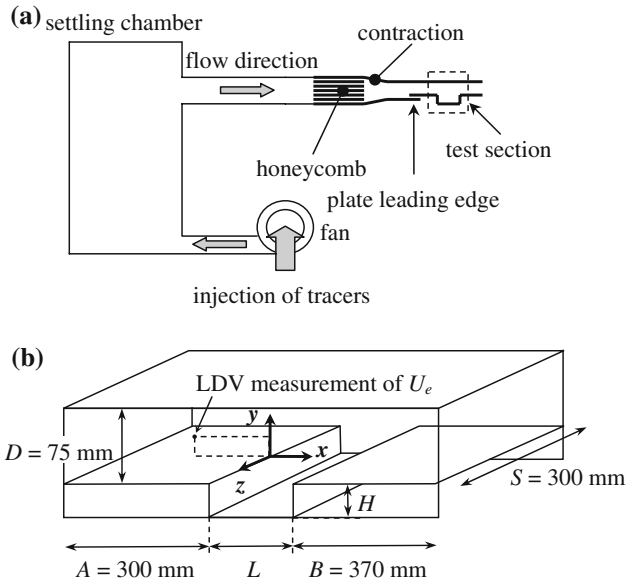

Fig. 1 Experimental setup: **a** wind tunnel, **b** test section dimensions and coordinates system

terminated with honeycomb and a contraction drives the flow toward the experimental facility, which consists of a test section containing a flat plate beginning with an elliptical leading edge, in order to fix the boundary layer origin. The length of the plate is $A = 300$ mm providing an established laminar boundary layer at the cavity upstream edge. To reduce light wall reflections, the whole test section is made of antireflection glass 2 mm in thickness. The cavity height is varied between $H = 25$ and 150 mm. Its span $S = 300$ mm is constant because the cavity ends in this direction are the wind tunnel vertical walls (Fig. 1b). In addition to the Reynolds number, two other dimensionless numbers are defined: the span ratio, $F = S/H$ (span over height) studied from 2 to 12, and the cavity aspect ratio, $R = L/H$ (length over height) from 0.25 to 2.5. This latter ratio can be changed continuously by moving the glass pieces consisting in the downstream wall of the cavity and the downstream plate, which has a length $B = 370$ mm. The flow is incompressible since the maximum Mach number is lower than 0.01. At the wind tunnel outlet, the flow is rejected inside the experimental room.

The choice of a relevant length scale to build a Reynolds number is of first importance. Many authors working with compressible conditions (Forestier et al. 2003) chose a Reynolds number built on the momentum thickness δ_2 of the laminar boundary layer upstream of the cavity, which is the length scale for the shear layer initial development, and the upstream external velocity U_e. In the present work, that Reynolds number $Re_{\delta,2}$ is between 71 and 180, corresponding to external velocities from 0.57 to 2.77 m s^{-1}. If we consider the development of the shear layer above the cavity, the amplitude of its oscillations increases with the distance from the upstream edge of the cavity. Then, the cavity length L is pertinent for selection of linearly unstable modes in the shear layer. As a consequence, the relevant Reynolds number is Re_L. In the present study, it varies from 860 to 36,900. If we focus on the flow development inside the cavity, the confinement between the upstream and downstream walls, distant of L, and the confinement between the bottom of the cavity and the shear layer, distant of H, lead to define an additional Reynolds number Re_H, here from 1,150 to 36,800. As it has been shown (Brès and Colonius 2008), the development of an unstable three-dimensional unsteady mode inside the cavity with an oscillation frequency based on the cavity height H is comparable in all configurations, suggesting that H is the most appropriate scale to characterize the three-dimensional flow development. Then, that latter Reynolds number will be chosen and its relevance for the development of instabilities will be confirmed hereafter. Three independent dimensionless numbers are thereafter necessary for the cavity flow description, respectively, the Reynolds number based on cavity height $Re_H = \rho U_e H/\mu$, the aspect ratio $R = L/H$, and the span ratio $F = S/H$.

The external velocity is measured with laser Doppler velocimetry 102 mm upstream of the cavity and 25.5 mm above the flat plate. This point of measurement is in the external flow sufficiently upstream of the cavity to avoid any perturbation from the instability developing above the cavity. The origin of the coordinate system is set at the upstream edge of the cavity at mid-span, the x-axis is the flow direction, the y-axis is normal to the upstream wall where the boundary layer develops, and the z-axis is along the cavity span. It has been checked that the test section upper wall, located at $D = 75$ mm above the cavity, has no influence on the shear layer developing on the cavity and, as a consequence, no influence on the flow. The thickness of the boundary layer developing on this wall has no influence on the external flow along the longitudinal and spanwise directions. It has been shown for backward facing step flows that the influence of the upper wall affects the flow from 10 cavity heights downstream of the beginning of the step. The cavity under investigation is not a shallow cavity (for $L/H > 5$), where the shear layer tends to attach the cavity floor. However, in that configuration, the development and propagation of large-scale vortices appear to be relatively unaffected by confinement effects. In the present study, it will be even more so given the maximum aspect ratio of 2.5.

Hereafter, the expressions "upstream" and "downstream" will refer to the external velocity direction. Flow visualizations by tracer injection are carried out with fog obtained with a low density smoke generator. As a result, the observed structures are streaklines of fluid injection inside the cavity and not the streamlines themselves. The identity between streaklines and streamlines is valid only for stationary flows, which is not strictly the case for present measurements. However, the Reynolds number is sufficiently low and the velocity inside the cavity is small enough to ascertain that visualizations show flow structures in well-seeded regions. This has been confirmed by comparisons with PIV measurements (Faure et al. 2008). Finally, the flow injection inside the cavity gives information on the flow dynamics and the developing structures.

The light source is a 5 W argon-ion laser tuned to the blue wavelength (488 nm). The laser beam provides, by passing through a cylindrical lens, a sheet whose thickness is 0.25 mm. The image recording system consists of a 10-bit camera with 1,032 × 778 pixels and a frequency of 20 Hz. The camera has a complete view of the cavity span. For each cavity geometry, the position of the (x, z) visualization plane is set to a relative vertical position $y^* = y/H = -0.3$ (Fig. 2). An exploration of the cavity along the y-axis points out the overall annular flow pattern. That particular value of y^* is retained, for comparison of

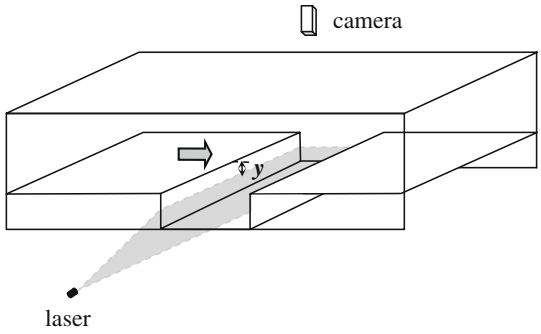

Fig. 2 Visualization in a (x, z) plane inside the cavity

different cases, because a vortex of spanwise axis is always present in the upper part of the cavity. The recording time is 25 s, which is sufficient to capture the flow dynamics unsteadiness. The repeatability of flow visualizations has been checked by recording different image series with different wind tunnel runs, and by testing different smoke injections. The external flow is established and uniformly seeded with smoke when the images are recorded. Note that if the observation time is too long, there is a saturation of the cavity with smoke and no dynamical flow pattern can be identified anymore.

3 Flow morphology

The three-dimensional character of the cavity flow has been recognized in previous studies (Faure et al. 2007; Brès and Colonius 2008). The shear-layer oscillations present amplification along the cavity length and interact with the downstream edge of the cavity (Fig. 3b). It results in a periodic injection of the external flow inside the cavity, carried along a primary vortex of spanwise axis. A secondary counter-rotating vortex of spanwise axis is also identified for long ($R > 1.25$ Fig. 3a) or short ($R < 0.75$ Fig. 3c) cavities. In that latter case, the vortex is placed in the lower half of the cavity while in the former case it forms in the upstream half of the cavity. These primary and secondary vortices are unsteady for most configurations. In the following part, the existence and properties of additional spanwise instabilities are discussed in relation with the Reynolds number, aspect ratio and span ratio. Three behaviors are identified: the absence of any spanwise row of vortices (Fig. 3d), spanwise instability vortices aligned in rows in the upper and lower cavity edges (Fig. 3e) or the presence of an isolated pair of vortices near the upstream edge (Fig. 3f). These instability vortices are carried off toward the lateral sides of the cavity by a spanwise flow, coming from the cavity sides toward the centerline and forming four recirculation cells (Fig. 3d–f). The development of these three-dimensional instabilities is caused by perturbations on the basic flow. It has been shown that these instabilities are essentially independent of the Mach number (Brès and Colonius 2008).

3.1 Absence of spanwise row of vortices

Let us consider first cases where no spanwise row of vortices is present, that is the case when the advection flow velocity inside the cavity is not strong enough to destabilize the wall boundary layers. That advection velocity comes from the primary vortex, developing along the cavity span, which places in the downstream part of the cavity. Figure 4 shows the dynamical structures for $Re_H = 2{,}967$ and $R = 1$ in the visualization plane; the external flow, passing above the cavity, is from the bottom to the top of the figure. We note the downstream cavity shear-layer interaction with the cavity, producing seeding injection. The tracer is advected inside a main vortex, developing in the (x, y) plane, that is identified as the upstream cavity wall white line. The inner part of the cavity points out a flow coming from the sides to the centerline. Thus, there is a coupling between the left and right sides and the central part of the flow, leading to four low velocity recirculation cells inside the cavity (Faure et al. 2007).

Another type of flow without row of vortices shows two corner spiral vortices near the cavity spanwise sides, the left one being in a shadow zone (Figs. 5, 6). This type of flow has been reported and studied extensively in lid-driven cavities (Chiang et al. 1997; Migeon et al. 2003), for a Reynolds number of 1,000. The corner vortices are the consequence of a fluid transport from the sides into the primary vortex core, due to an Ekman layer. Note that in the present investigation, they have been identified only for the span ratio $F = 3$ and small aspect ratios $R < 1$. They may be present for other cases, but the laser plane, located at $y^* = -0.3$, is not necessarily perpendicular to the spiral vortex axis, preventing their visualization. In some cases, the effect of a limited flow seeding near the cavity span sides can also affect their observation.

3.2 Presence of spanwise instabilities

Figure 7 shows the cavity flow for a configuration with a row of mushroom-like patterns near the upstream cavity edge. Note that views in three different planes are not taken at the same time. The mushroom-like seeded patterns are visualizations of pairs of counter-rotating vortices whose axes are orthogonal to the observation plane (Fig. 7a, b). These vortices are also observed near the downstream cavity edge, and, for that case with a single vortex of spanwise axis spreading over the cavity section, this pattern is found for different relative position y^* inside the cavity,

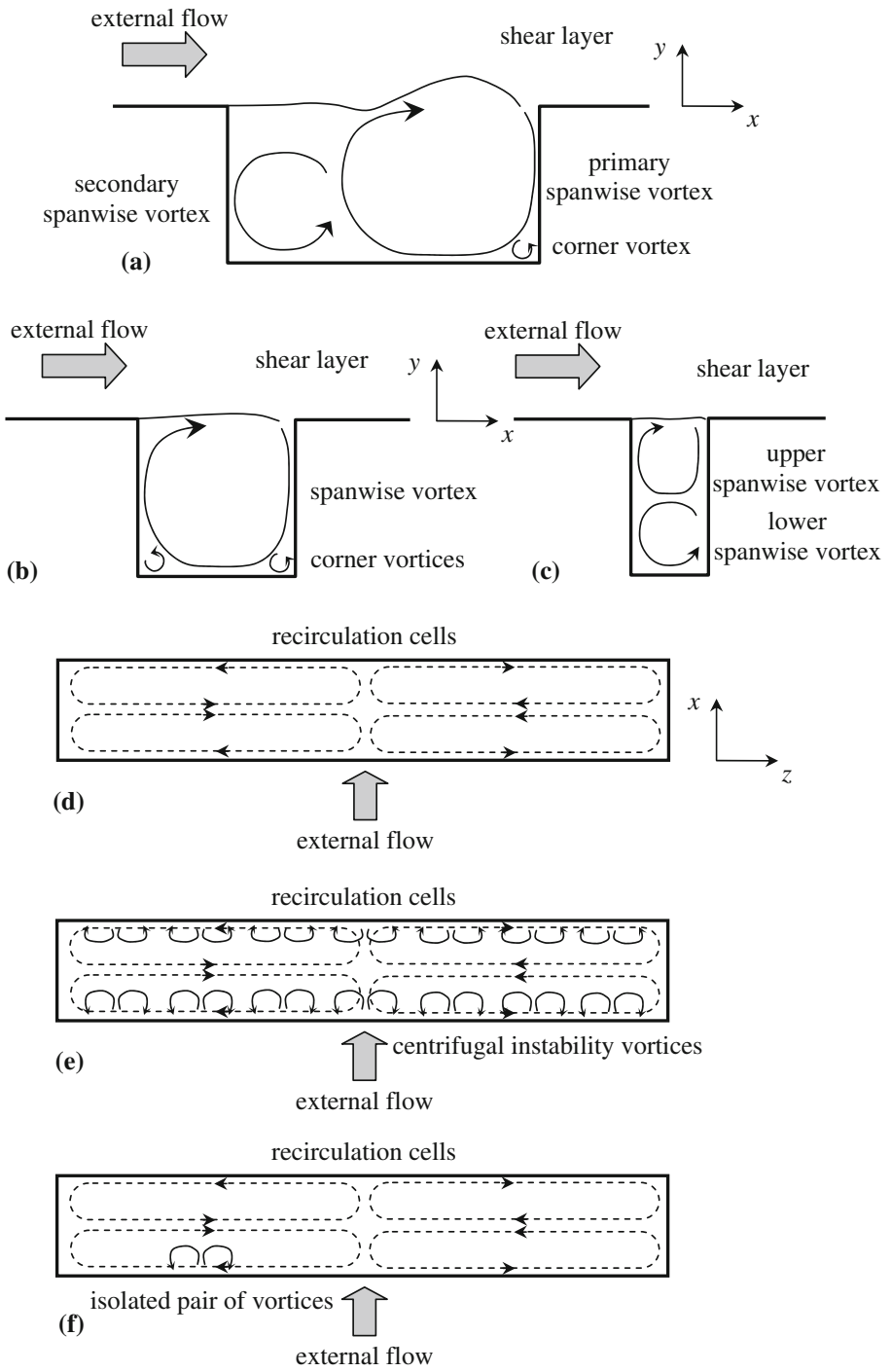

Fig. 3 Sketch of the cavity flow dynamics in a (x, y) plane for: **a** $R > 1.25$, **b** $1.25 \geq R \geq 0.75$, **c** $R < 0.75$ and in a (x, z) plane with: **d** the absence of any spanwise row of vortices, **e** spanwise instability vortices aligned in rows and **f** the presence of an isolated pair of vortices

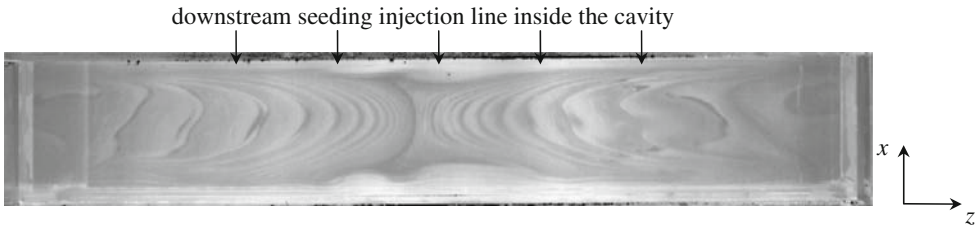

Fig. 4 Visualization for $F = 6$, $R = 1$ and $Re_H = 2{,}967$

Fig. 5 Visualization for $F = 3$, $R = 0.25$ and $Re_H = 10{,}632$

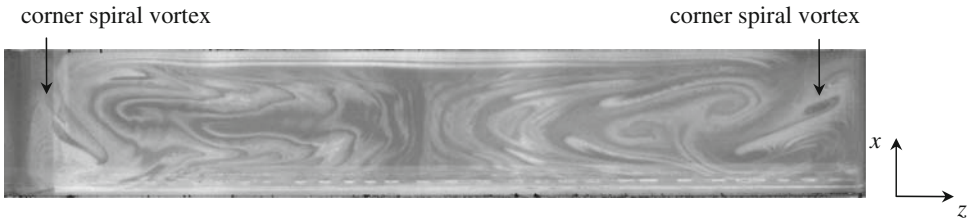

Fig. 6 Visualization for $F = 3$, $R = 0.5$ and $Re_H = 4{,}120$

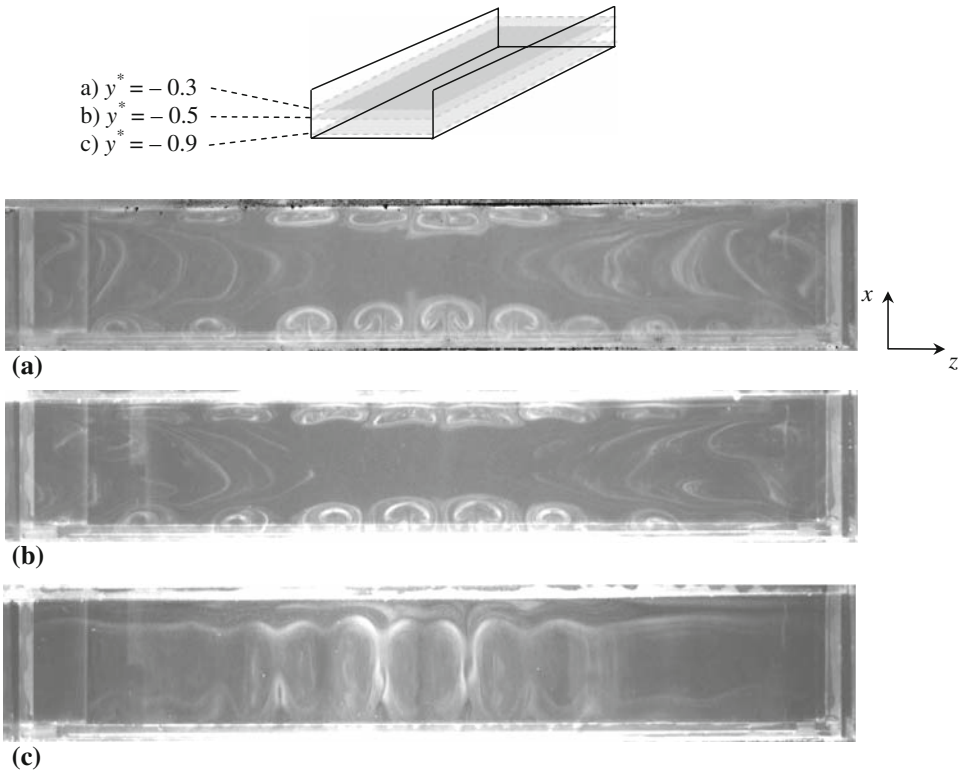

Fig. 7 Visualization for $F = 6$, $R = 1$ and $Re_H = 4{,}230$ for **a** $y^* = -0.3$, **b** $y^* = -0.5$ and **c** $y^* = -0.9$

evidence that they are forming a loop inside the cavity. Particularly for $y^* = -0.9$, near the cavity bottom, the row of vertical oval patterns is the intersection of tire-like instabilities with the laser plane (Fig. 7c). For that Reynolds number, between 9 and 11 pairs of vortices are observed. Note that the spacing between pairs is not constant, as mentioned by Finnis and Brown (1997). The vortices are smaller near the cavity sides (left and right part in Fig. 7a), where the spanwise flow is dominant, which evidences that the spanwise flow tends to stabilize the cavity boundary layer, preventing the development of instabilities.

For a larger Reynolds number (Fig. 8), the upstream row is still present, but is a little more deformed, while the downstream row tends to flatten on the wall. For that configuration, between seven and nine pairs of vortices are observed near the upstream edge. They are also identified near the downstream cavity edge, evidence of their annular shape (Fig. 8).

The issue of the flow properties description previously addressed with a dimensional analysis can be raised if one observes the cavity flow for the same aspect ratio and the same Reynolds number, but for two different span ratios (Figs. 9, 10). For $F = 6$, there is a well organized row of mushroom-like patterns around the center span of the cavity (Fig. 9) while there is no more row of instabilities for $F = 2$ (Fig. 10).

An incompressible, isothermal, unsteady three-dimensional direct numerical simulation (DNS) has been realized for the particular case $F = 6$, $R = 1$ and $Re_H = 4{,}230$ with

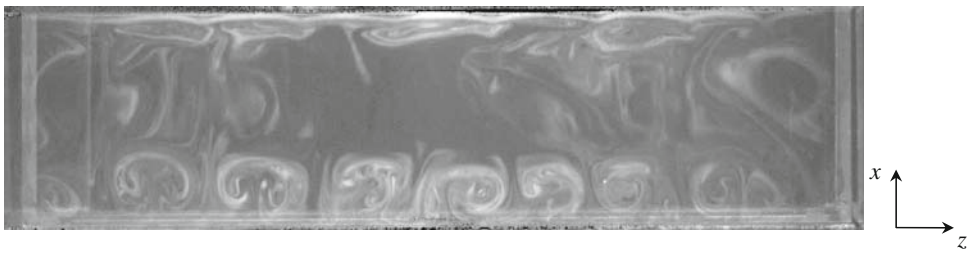

Fig. 8 Visualization for $F = 6$, $R = 1.5$ and $Re_H = 4{,}230$

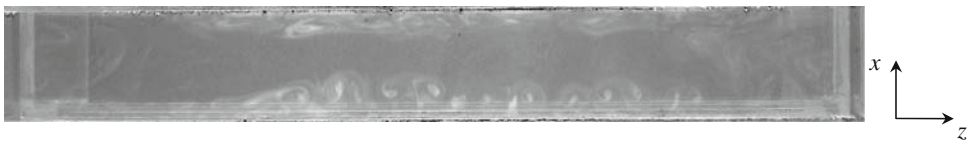

Fig. 9 Visualization for $F = 6$, $R = 0.75$ and $Re_H = 9{,}070$

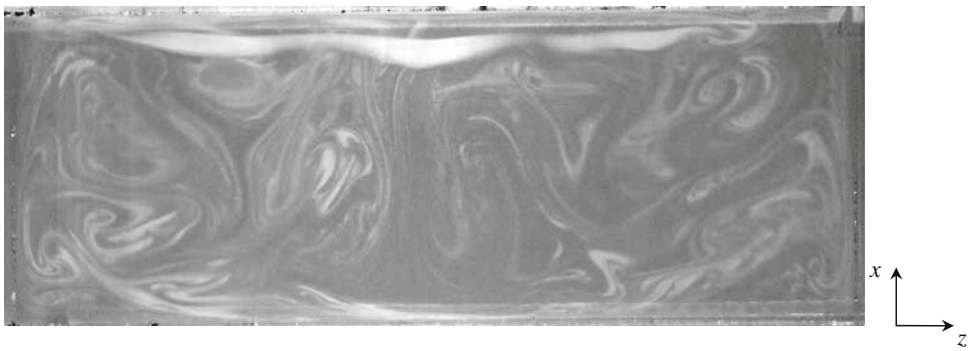

Fig. 10 Visualization for $F = 2$, $R = 0.75$ and $Re_H = 9{,}070$

the Olorin code developed in LIMSI. Navier-Stokes equations are discretized following a finite volume approach on a staggered structured grid with a second order approximation in time and space. Advection fluxes are calculated with a quadratic upstream interpolation for convective kinematics scheme (Leonard 1979). The discretized Navier-Stokes equations are implicited on viscous terms leading to the set of Helmholtz equations resolved by an incremental alternating direction implicit method (Hirsch 1987). The incompressibility is realized with a usual prediction/projection method. The projection step leads to resolve a Poisson equation for the pressure with a relaxed Gauss-Seidel method, coupled with a multigrid method to accelerate the time convergence of calculation (Gadoin et al. 2001). The grid is 256 × 128 × 128 nodes with clustering of points spacing near the walls in the cavity and shear layer. The computational domain extends several cavity heights upstream and downstream. Top, bottom and lateral boundaries of the domain are rigid and a laminar boundary layer develops upstream of the cavity. The simulated velocity field is carried out over 40 s after the flow is converged in a statistical sense. The recording frequency is 30 Hz. It is representative of the dynamical scales inside the cavity. Figure 11 shows the three-dimensional view of the cavity with the helicity of the velocity field defined as:

$$\mathcal{H} = \vec{V} \cdot \vec{\omega}$$

with $\vec{V}$ the velocity vector, $\vec{\omega} = \overrightarrow{\text{curl}}\ \vec{V}$ the vorticity vector.

If one compares this result (Fig. 11) with the flow visualization (Fig. 7a), a very good agreement is found, which confirms the accuracy of the visualizations. The pair of positive and negative helicity contours corresponds to pairs of centrifugal instability vortices. A comparison in the (x, z) plane located at $y^* = -0.3$ is provided in Fig. 12. Note that the number of centrifugal instability vortices is a little more important in the simulation (between 12 and 14) than in the experiment (between 9 and 11), but their sizes are comparable. This difference is probably due to the comparison of two instantaneous fields at a different time. In addition, the lateral parts of the cavity along the span might be not correctly seeded in the visualization and we could miss some pair of instabilities. This simulation is also in good agreement with the calculation of Brès and Colonius (2008) obtained for a similar configuration with a compressible code with a linear stability analysis to search

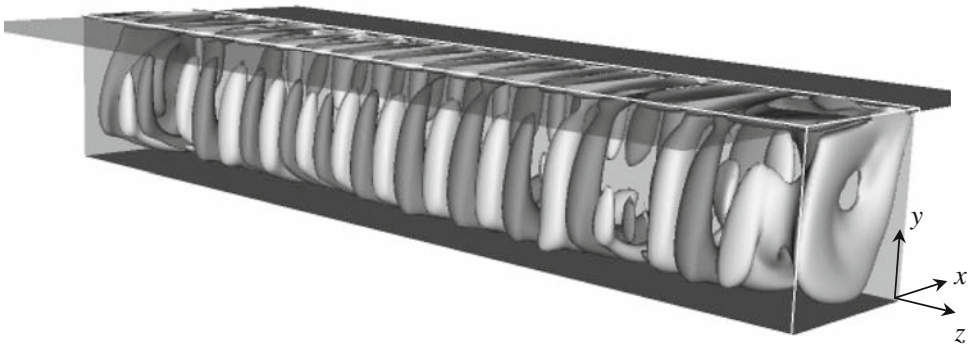

Fig. 11 Helicity obtained by DNS for $F = 6$, $R = 1$ and $Re_H = 4{,}230$

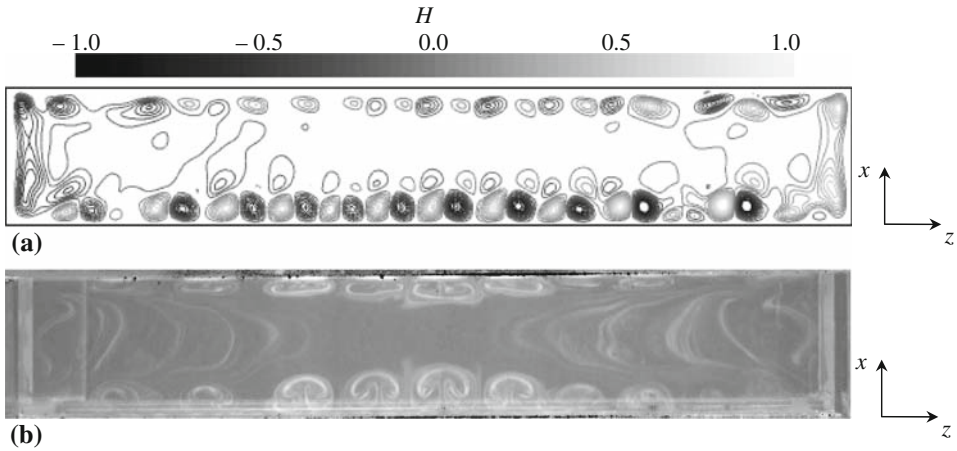

Fig. 12 Spanwise instabilities development for $F = 6$, $R = 1$ and $Re_H = 4{,}230$; **a** helicity of the numerical simulation and **b** flow visualization

for three-dimensional global instabilities of the two-dimensional mean flow, with lateral periodic boundary conditions. For that latter computation, the comparison with the visualization is realized in the central part of the cavity and does not take into account the effects of the lateral sides.

3.3 Secondary spanwise instabilities modulation

The row of instabilities is also subject, for some parameters, to present a second order time-dependent modulation of its amplitude (Fig. 13). The mechanism involves two adjacent pairs of mushroom-like structures. When one of these pairs is well developed in the z extension, its neighbor shows a narrow and elongated shape along the x-axis. Then the first one is crushed and ejected in the central part of the cavity, while the latter is increasing in z and decreasing in x extension, down to the upstream edge of the cavity. The mechanism of stability exchange is then repeated periodically in time with a given period of around 1 s. This time-dependent secondary instability is observed only for $F = 12$, for any aspect ratio where a row of instability is present and $R > 1$. To the authors' knowledge, this result has never been mentioned in previous studies on open cavity flows or lid-driven cavity flows.

3.4 Isolated unsteady instabilities

Figure 14 points out a case where the pairs of vortices are not organized into a row, but rather form unsteady isolated pairs. In this figure, only one pair of vortices is present on the left side of the image near the upstream wall with no counterpart close to the downstream wall. This suggests that the annular shape of the centrifugal instability is lost.

3.5 Transitional flow

For high Reynolds numbers, no row of identified flow patterns is observable because the flow is transitioning toward turbulence (Fig. 15). Centrifugal instability vortices are, however, still present but their patterns are no more stable structures. They evolve in coherent large-scale structures, which cannot be identified with flow visualization because of tracer diffusion. As it can be thought, the Reynolds number is not the only parameter to define the

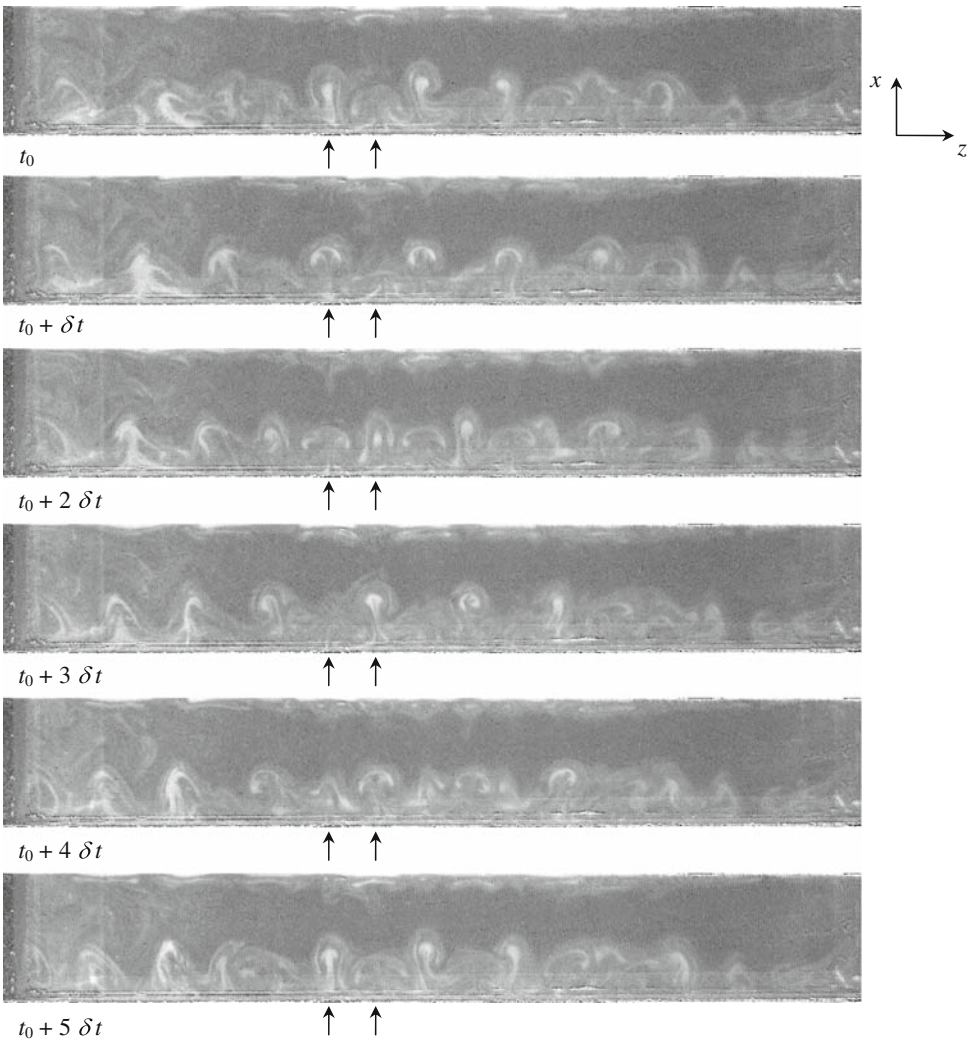

Fig. 13 Visualization for $F = 12$, $R = 1.75$ and $Re_H = 2\ 660$, with time interval $\delta t = 0.2$ s (the *arrows* note two neighboring pairs of vortices to point out their amplitude modulation with time)

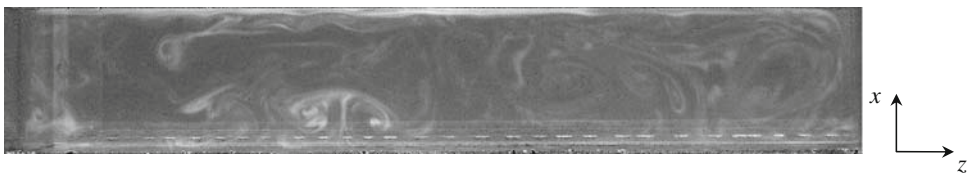

Fig. 14 Visualization for $F = 3$, $R = 0.5$ and $Re_H = 15{,}000$

Fig. 15 Visualization for $F = 6$, $R = 1.5$ and $Re_H = 7{,}500$

presence or absence of these vortices, since the cavity geometry plays an important role.

The existence domain of structured spanwise vortices is thus limited by a domain with no spanwise row of vortices, for lower Reynolds numbers, and a domain of transition of these vortices toward a turbulent flow, for much higher Reynolds numbers. The limiting thresholds are established and discussed in the following section.

4 Properties and data reduction

4.1 Influence of the span ratio

Figure 16 ascertains the domain of existence of centrifugal instability vortices, as functions of Reynolds number Re_H and aspect ratio R, for different span ratios F. For $F = 12$–3 (Fig. 16a–c), the region where instabilities are present in the plane (R, Re_H) is forming a compact domain, which is not the case for $F = 2$ (Fig. 16d), where there are two distinct regions with the presence of spanwise instabilities linked by a zone with isolated pairs instead of rows of instabilities. For this case, this particular behavior may be caused by the influence of lateral confinement on the generation mechanism of the centrifugal instability vortices. The centrifugal instability vortices development can be understood as a three-dimensional perturbation of a two-dimensional mean flow. The secondary spanwise instability is only present for $F = 12$ and for every aspect ratio $R > 1$ (Fig. 16a). It might be thought that the time-dependent secondary instability of the row is due to a balance between the spanwise recirculation and the primary cavity vortex expansion, since a secondary vortex exists for $R > 1$. Another interesting result, under the limitation of the investigation domain, is that the lower threshold of existence of instabilities is independent of Re_H for $R \geq 1.5$ (Fig. 16a–c). This suggests that the number of vortices of spanwise axis inside the cavity strongly modifies the instability process. Previous studies of lid-driven cavities, available for $F = 3$ and $R = 1$, show the development of centrifugal instability vortices for $Re_H > 1{,}300$ (Chiang et al. 1997, 1998) or $Re_H > 1{,}000$ (Koseff and Street 1984a, b, c), which is consistent with the present study since the centrifugal instability vortices are identified for the first Reynolds number measured, which is 4,120 (Fig. 16c). Studies for $F = 2$, $R = 1$ and $Re_H = 1{,}000$ and $F = 4$, $R = 2$ and $Re_H = 500$ (Migeon et al. 2003) do not show any development of centrifugal instability vortices, which is also consistent with the present measurements. We can say that the confinement effects, resulting in a division of the existence domain of instabilities, are limited to span ratios $F < 2$. If we get rid of the span ratio $F = 2$, a unique domain of existence of centrifugal instability vortices is found, also considering isolated vortices, with the same thresholds for any span ratio (Fig. 17). Thus, the analysis of the flow dynamical properties inside the cavity

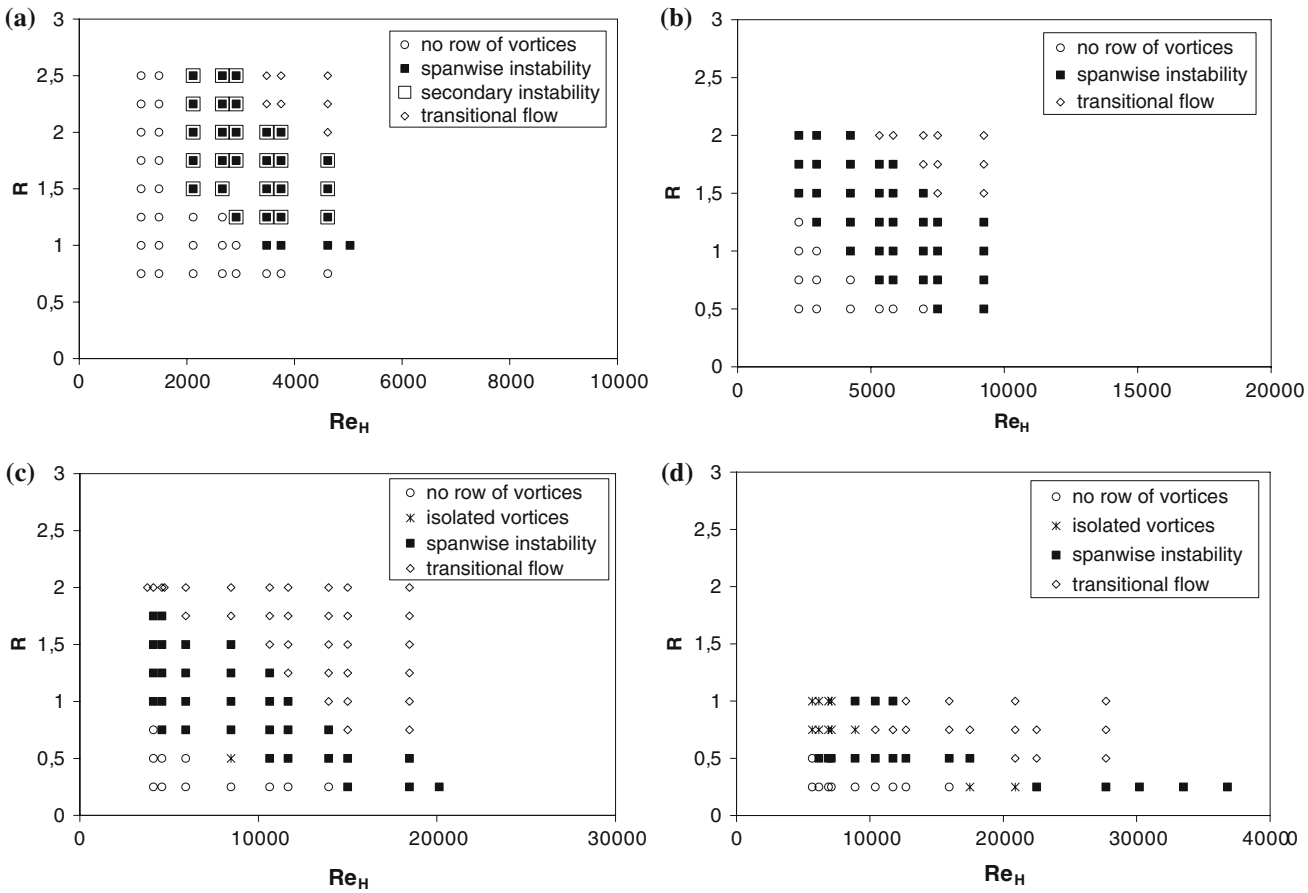

Fig. 16 Existence diagram of centrifugal instability vortices versus Re_H for **a** $F = 12$, **b** $F = 6$, **c** $F = 3$ and **d** $F = 2$

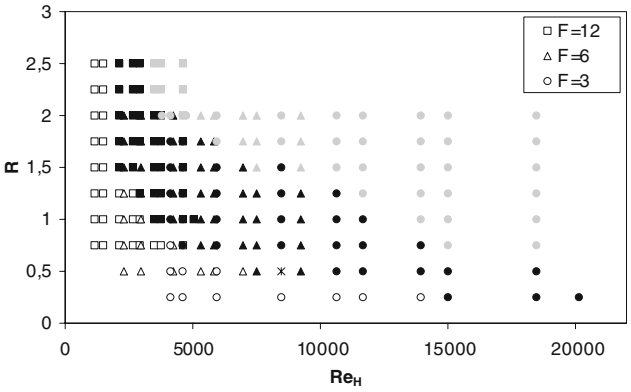

Fig. 17 Existence diagram of centrifugal instability vortices versus Re_H for $F = 12$ (*squares*), $F = 6$ (*triangles*), $F = 3$ (*circles*) with the following notation conventions: *hollow symbol* no row of vortices, *full symbol* spanwise instability, *cross* isolated vortices for $F = 3$, *gray symbol* transitional flow

can be reduced to two dimensionless numbers, say Re_H and R, for large span ratio cavities ($F \geq 3$), not considering the secondary instability. In some regions of the stability diagram (Fig. 17), near the upper limit of stability, there is a superposition of hollow and full symbols, for instance, for $R = 2$ and $Re_H = 3{,}790$, where hollow circles are mixed with full squares. It must be due to the uncertainty in the parameters setting. Notice that the cavity height H is the appropriate scale to describe the cavity flow instability development, while the cavity length L is the appropriate scale for the shear-layer development.

4.2 Number of centrifugal instability vortices

Figure 18 shows the number of pairs of centrifugal instability vortices present simultaneously inside the visualization plane versus Re_H. Cases with vortices rows as well as cases with isolated pairs of vortices are considered (then, $N = 1$). Limiting cases where vortices are not present are also marked (then, $N = 0$). As the vortices are evolving with time, the uncertainty on their number is estimated to ± 1 and the figures plotted are averaged values on the recorded sequences. For each span ratio where a complete cycle of appearance, presence and vanish of instabilities is investigated experimentally, we note an increase followed by a decrease of the number of pairs of vortices. This is the proof that the appearance-vanish cycle is a continuous phenomenon driven by the external velocity U_e. The geometry is also important since there is an aspect ratio for which the vortices number reaches a maximum. We can notice in Fig. 18a and b that this maximum number of spanwise pairs of vortices is found for $R = 1$. This must be connected to the presence of a main round vortex of spanwise axis inside the cavity, which provides a best radius of curvature with respect to wall confinement. There is a drop of the number of vortices for $F = 3$ (Fig. 18c), the maximum being get for $R = 1.25$. The same comment is done for $F = 2$ with a lower number of vortices (Fig. 18d). That decrease of the number of vortices inside the cavity with span ratio increase points that the three-dimensional flow is a phenomenon preventing the formation of centrifugal instability vortices.

As very few data concerning the number of centrifugal instabilities are available, these measurements deserve comparison with the results of Koseff and Street (1984a) for a lid-driven cavity. They found 8 pairs of centrifugal instability vortices for $F \leq 3$, $R = 1$, $Re_H = 3{,}000$ and 11 pairs for $Re_H = 6{,}000$. The present measurements give four pairs of instability vortices, respectively, for $F = 3$, $R = 1$, $Re_H = 4{,}120$ and 5,930. If we can draw a conclusion from the comparison between these two Reynolds numbers, it can be said that oscillations of the shear layer affect the flow organization inside the open cavity, which is different from a lid-driven cavity. However, we note here 8 pairs for $F = 6$, $R = 1$ and $Re_H = 4{,}230$ and 10 pairs for $F = 6$, $R = 1$ and $Re_H = 5{,}830$, results close to Koseff and Street's observation. The comparison of our measurements with the development of a shear-layer-driven cavity flow, for $R = 1$ and $Re_H = 6{,}970$, presents a good agreement (Brès and Colonius 2008). As there is a span periodicity in their simulation, these authors found five pairs of centrifugal instability vortices, to compare with the five pairs obtained in the central third of the span in present measurements (Fig. 12). The difference in the number of vortices between lid-driven and shear-layer cavity flow could suggest that the latter, with the development of a shear layer, is more affected by the span ratio than the lid-driven cavity.

The viscous effects on the stability development inside the cavity are stronger for small aspect ratios R and small span ratios F. This could explain the peculiar existence diagram for $F = 2$ (Fig. 16d) with two distinct regions and cases where isolated vortices are present. Similarly, viscous effects get stronger for small aspect ratios R, which could explain the absence of secondary instability for $F = 12$ and $R = 1$ (Fig. 16a). An attempt of description of the instability generation process could be observed as follow, increasing the cavity dimensions (span ratio F). The viscous effects tends to limit the development and number of spanwise instabilities for $F = 2$ (Fig. 18d), there is a development of spanwise instabilities as a row of pairs of vortices for $3 \leq F \leq 6$ and for $F = 12$ the secondary spanwise instability modulation appears.

4.3 Wavelength

As the centrifugal instability vortices are developing along the cavity span, their number is strongly tied to their

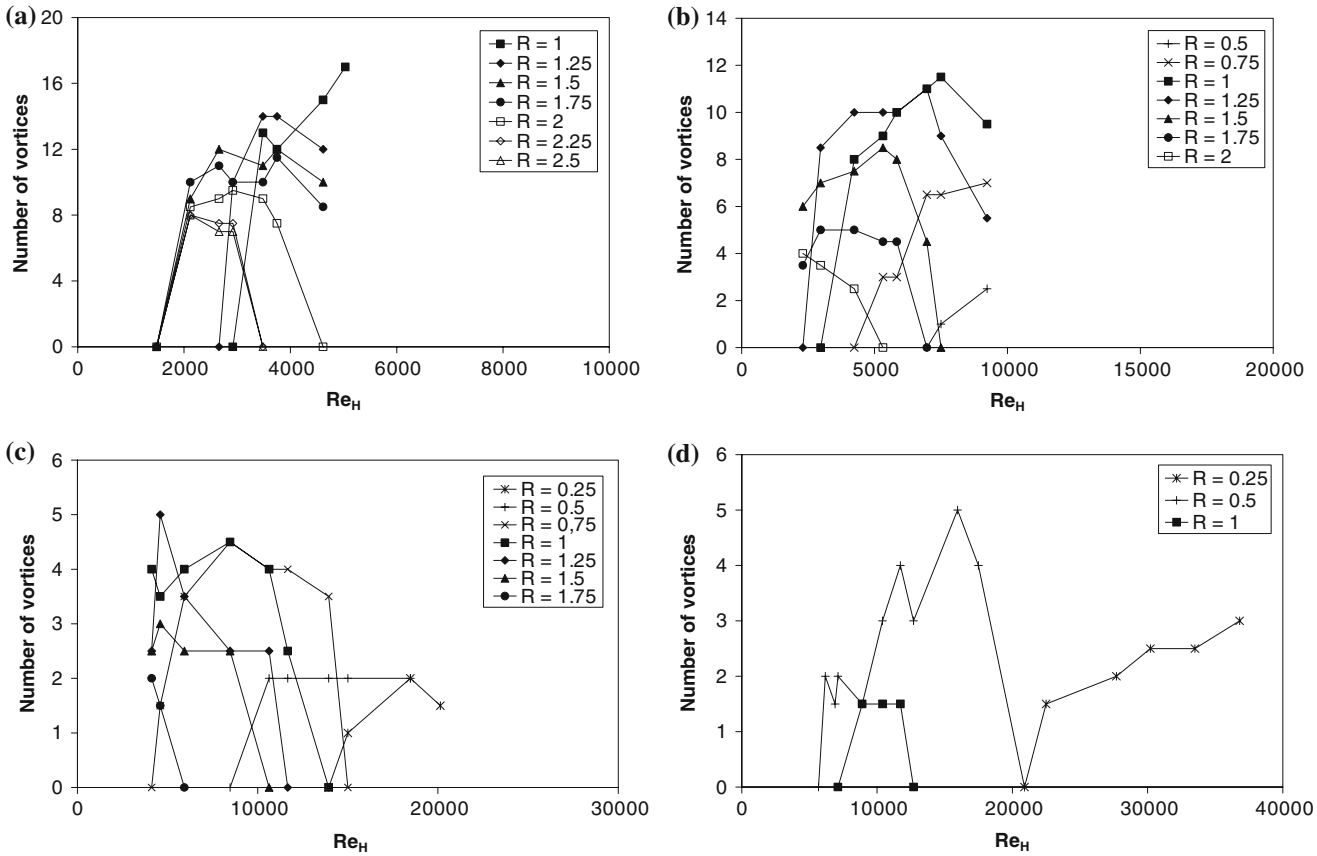

Fig. 18 Number of centrifugal instability vortices versus Re_H for **a** $F = 12$, **b** $F = 6$, **c** $F = 3$ and **d** $F = 2$

wavelength. However, the pairs of vortices are not always adjoined, so the measurement of an averaged wavelength from flow visualizations seems relevant. Its uncertainty is ±2 mm. Figure 19 presents the development of the spanwise wavelength λ, corresponding to the distance between two pairs of vortices, versus the Reynolds number Re_H. Note that the wavelength is plotted only when a row of instabilities is present, thus cases with isolated unsteady instabilities are not considered. As we noted previously, the spacing between vortices is not always constant, and the estimated wavelengths must be understood as maximum averaged values. The wavelengths have been measured on the images recorded for each geometrical and wind tunnel parameter. An automatic research of the wavelength can be achieved, for example, with a Fourier transform of the image of flow visualization to get the more significant wave number. However, this is difficult to realize because small scale structures appear as the most powerful components in a rather broadband spectrum, and finally the search is conducted by visual analysis. The general trend observed in Fig. 19 is an increase of the wavelength with the aspect ratio R except for $F = 2$ where three-dimensional effects on the mean flow are very strong. It means that larger instabilities, along the z-axis, are present for long cavities. The instability generation is driven by a three-dimensional coupling between the axial and span directions. Note that for large span ratios ($F = 12$, 6) the wavelength can be greater than the cavity height. The wavelength tends also to increase slowly with the Reynolds number Re_H, for most of the cases, confirming an influence of the external flow on the instabilities generation.

An estimate of the wavelength measured by Koseff and Street (1984a) gives $\lambda/H = 0.38$ for $F \leq 3$, $R = 1$ and $Re_H = 3{,}000$ and $\lambda/H = 0.27$ for $Re_H = 6{,}000$. Similarly, Freitas and Street (1988) provide $\lambda/H = 0.2 - 0.3$ for $F = 3$, $R = 1$ and $Re_H = 3{,}200$. In the present study, $\lambda/H = 0.78$ for $F = 3$, $R = 1$ and $Re_H = 4{,}120$ and $\lambda/H = 0.68$ for $F = 3$, $R = 1$ and $Re_H = 5{,}930$. As mentioned in the discussion on the number of instabilities vortices, the oscillations of the shear layer above an open cavity may affect the flow organization inside the cavity in a different way from a lid-driven cavity.

4.4 Spanwise drift velocity

It has been shown by Faure et al. (2007) that the spanwise instabilities are migrating from the cavity centerline outward the cavity sides. This drift motion is due to the

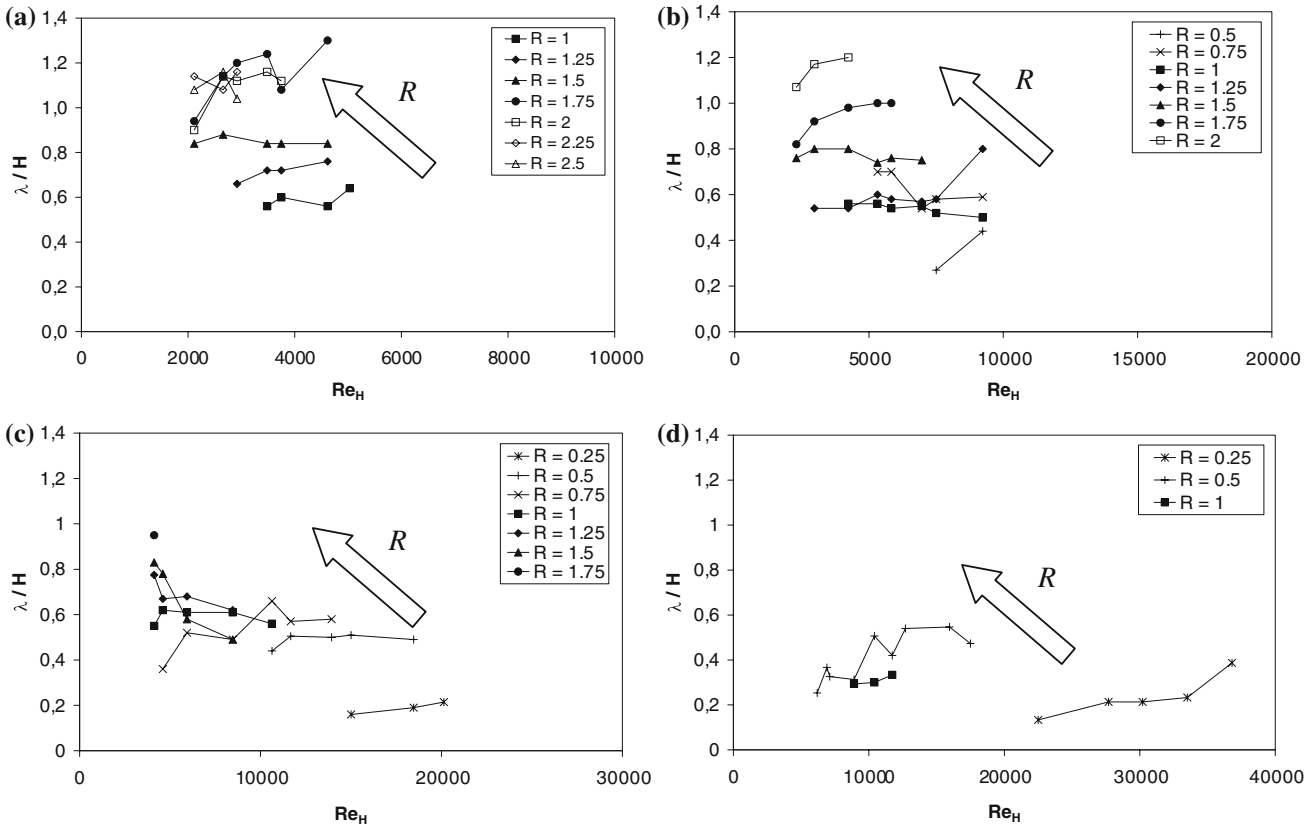

Fig. 19 Wavelength of the centrifugal vortices row versus Re_H for **a** $F = 12$, **b** $F = 6$, **c** $F = 3$ and **d** $F = 2$

spanwise flow in the inner part of the cavity from the sides toward the centerline. The spanwise drift velocity W_s is measured from space-time diagrams. They are built stacking, over each other, a horizontal line of the visualization chosen in a region where spanwise instabilities are present, at different successive times (dashed white line in Fig. 20a). On such diagrams, vertical lines are associated to stationary events, while oblique lines are associated to traveling patterns (Fig. 20b). If oblique lines are, moreover, straight lines, it means that the pattern is traveling at a constant velocity. As these lines have a slope between zero and a maximum value, we choose to characterize each configuration with a maximum spanwise drifting velocity W_s. That velocity can also be measured from a Fourier transform of the space-time diagram (Fig. 20c), where the spanwise drift velocities consist in a set of maxima around zero, limited by a maximum value (dashed white line, Fig. 20c). The measurement of W_s brings to 7.3 mm s^{-1} with both of these methods.

Another reason to choose the maximum spanwise drift velocity to characterize the span flow motion is that the drift motion is not symmetrical for all configurations. There is a shift of the symmetry axis from the centerline of the cavity. This shift is not an experimental artifact since it can be found for different successive wind tunnel runs and is reproduced in the numerical simulations. Note that the spanwise drift velocity W_s is very low in comparison with the external velocity, reaching a maximum value of 2% of U_e. This velocity W_s is also lower than the maximum advection velocity inside the cavity U_c which is generally 5% of U_e (Fig. 21):

$$\frac{U_c}{U_e} \leq 0.05 \quad \frac{W_s}{U_e} \leq 0.02$$

Let us now consider the variation of that drift velocity with Re_H, R and F. The general behavior is a global decrease of W_s/U_e with R, showing that short cavities help the drift flow. For $F = 12$ (Fig. 22a), the drift velocity tends to decrease when the Reynolds number increases except for $R \geq 2$. The drift velocity is generally greater for the lower Reynolds number Re_H where spanwise instabilities are present than for higher Reynolds numbers. For $F = 6$ (Fig. 22b), the drift velocity is almost constant versus Reynolds number. For $F = 3$ (Fig. 22c), the drift velocity decreases as Reynolds number increases. There is no spanwise drift velocity for $F = 2$ because of the very low number of spanwise instabilities. Notice that in numerical simulations with periodic boundary conditions, there is no more drift of the pairs of vortices. This would

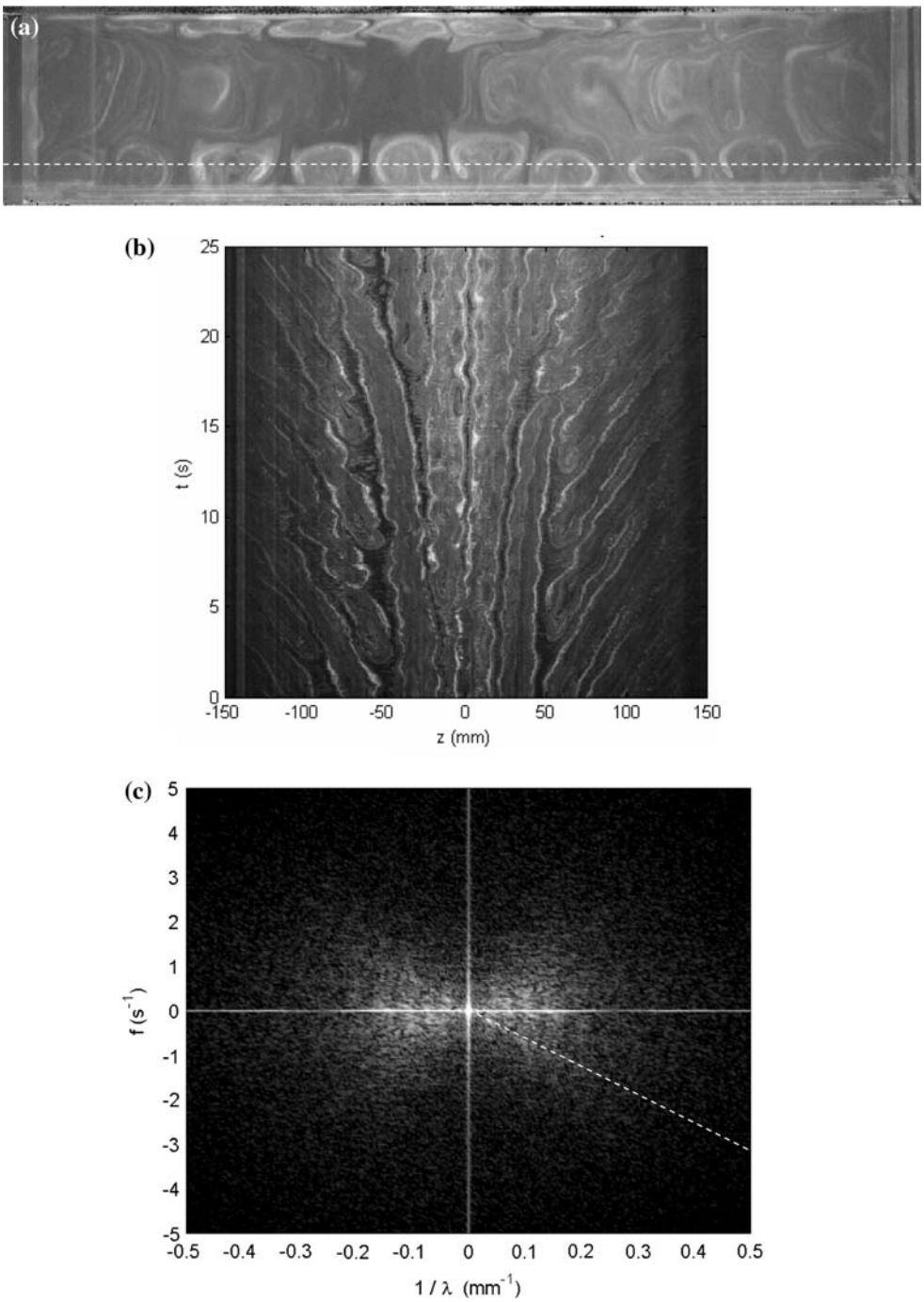

Fig. 20 **a** Visualization for $F = 6$, $R = 1.25$ and $Re_H = 5{,}320$, **b** corresponding space-time diagram and **c** Fourier transform of the space-time diagram

confirm that the mechanism of the drift originates in the lateral sides of the cavity, where an Ekman layer is present.

5 Conclusion

The flow inside a parallelepipedic cavity shows the development of different morphologies discussed in terms of the presence or the absence of centrifugal instability vortices. These flow instabilities are induced by the advection velocity and the flow curvature radius induced by a main vortex whose axis is the cavity span, and they are known as independent of the Mach number. For a squared section cavity and $Re_H = 4{,}230$, features of these instabilities present a good agreement with results obtained by a DNS of the flow. The pairs of vortices are not always present and the thresholds for their appearance and disappearance are identified. For low Reynolds numbers, they are not observed. This can be caused by an advection velocity that is not strong enough to destabilize the

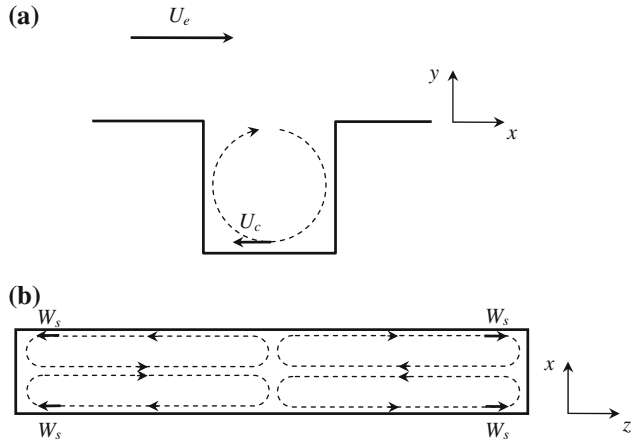

Fig. 21 Velocity scales **a** in a (x, y) plane and **b** in a (x, z) plane

boundary layer on the cavity walls. The spanwise flow coming from the cavity sides toward the centerline may also act as a stabilizing process preventing the formation of instabilities. For much higher Reynolds numbers, the flow is transitioning to a fully developed turbulent flow, and there are no more patterns resulting in spanwise instabilities. The geometry is also an important parameter in terms of existence of these instabilities. It has been pointed out that three dimensionless numbers are necessary to describe the flow, the Reynolds number and two geometrical ratios in order to take into account the three-dimensional flow features. However, the flow description can be reduced to two dimensionless numbers for $F \geq 3$.

The centrifugal instability vortices are generally developing in a spanwise row, but for some configurations, isolated pairs of vortices are observed particularly for low span ratios ($R = 2$, 3). The properties of the instabilities are also discussed in terms of drifting velocity toward the sides, wavelength and number. The spanwise drifting velocity is decreasing with aspect ratio. The wavelength of the row of instabilities mainly increases with aspect ratio. For cases with an established row ($F = 12$, 6), a maximum number is reached when $R = 1$. For lower span ratios, the number of pairs decreases rapidly since there is no more stable row but isolated pairs of vortices. It seems that the spanwise flow may prevent the centrifugal instability vortices generation.

The existence diagrams of instabilities point, for span ratios larger than 2, that the investigated zone where centrifugal instability vortices are present is forming a

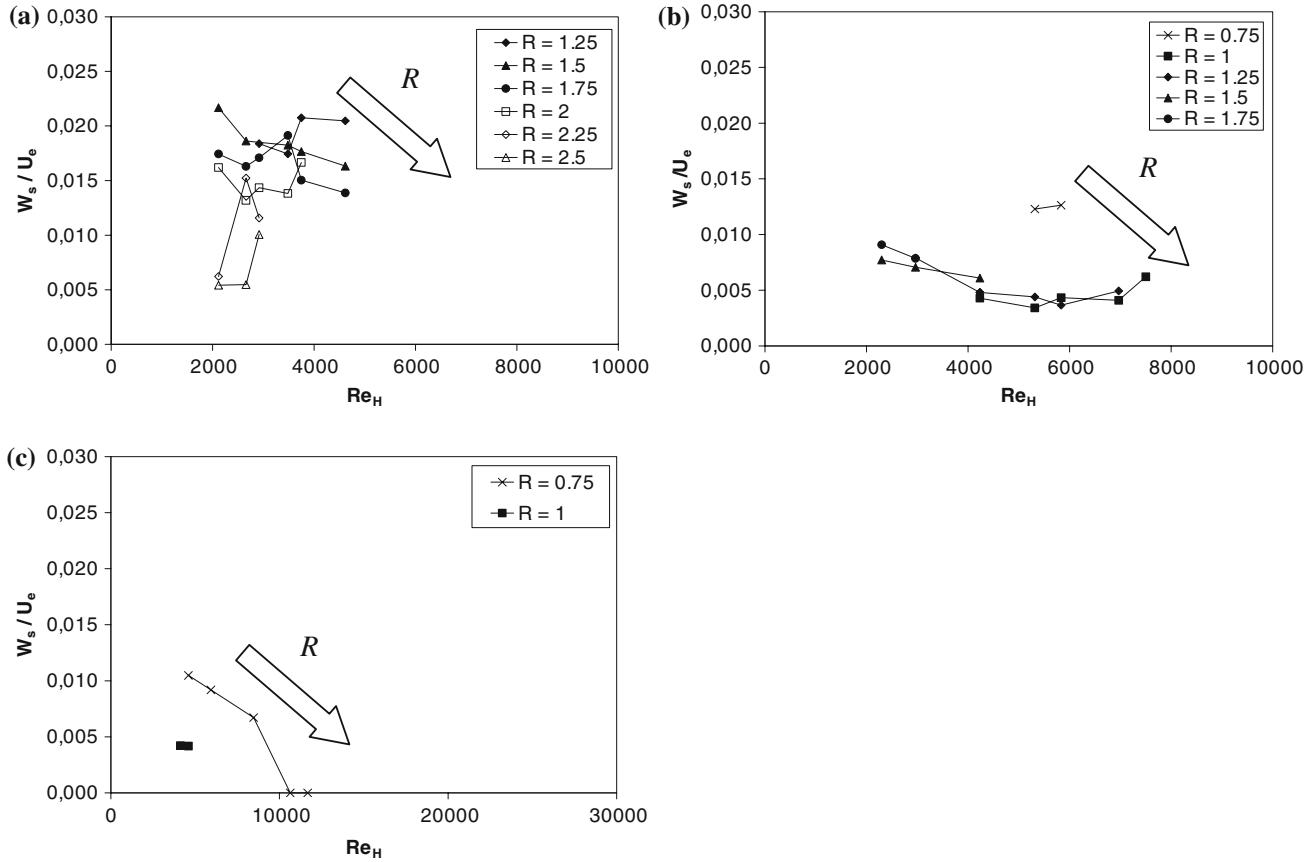

Fig. 22 Spanwise drift velocity W_s/U_e versus Re_H for **a** $F = 12$, **b** $F = 6$ and **c** $F = 3$

compact domain. This is not true for $F = 2$, where the existence domain is divided between two regions separated by a line where isolated pairs are observed. A similar division into two existence domains may also be relevant for higher span ratios, but for aspect ratios larger than 2.5, which have not been investigated. The lower threshold of existence of instabilities is independent of Re_H for $R \geq 1.5$, which suggests that the number of vortices of spanwise axis inside the cavity strongly conditions the instability process. The similarity behavior of the existence region of instabilities for different values of $F \geq 3$ is obtained with the Reynolds number built on cavity height. It seems that this dimension is the driving parameter for the cavity flow dynamics.

References

Aymer de la Chevalerie D, Fonteneau A, De Luca L, Cardone G (1997) Görtler-type vortices in hypersonic flows: the ramp problem. Exp Thermal Fluid Sci 15:69–81

Brès GA, Colonius T (2008) Three-dimensional instabilities in compressible flow over open cavities. J Fluid Mech 599:309–339

Chang K, Constantinescu G, Park SO (2006) Analysis of the flow and mass transfer processes for the incompressible flow past an open cavity with a laminar and a fully turbulent incoming boundary layer. J Fluid Mech 561:113–145

Chatellier L, Laumonier J, Gervais Y (2004) Theoretical and experimental investigations of low Mach number turbulent cavity flows. Exp Fluids 36:728–740

Chiang TP, Hwang RR, Sheu WH (1997) On end-wall corner vortices in a lid-driven cavity. J Fluids Eng 119:201–204

Chiang TP, Sheu WH, Hwang RR (1998) Effects of the Reynolds number on the eddy structure in a lid-driven cavity. Int J Numer Methods Fluids 26:557–579

Cui X (2004) Numerical simulations of the generation of Taylor-Görtler vortices during spin-down to rest in finite-length cylinders. Comput Fluids 33:603–621

Faure TM, Adrianos P, Lusseyran F, Pastur L (2007) Visualizations of the flow inside an open cavity at medium range Reynolds numbers. Exp Fluids 42:169–184

Faure TM, Defrasne A, Lusseyran F, Pastur LR (2008) Flow instabilities development inside an open cavity. 13th international symposium on flow visualization, Nice (France), 1–4 July 2008, paper ID 81

Finnis MV, Brown A (1997) The linear growth of Görtler vortices. Int J Heat Fluid Flow 18:389–399

Forestier N, Jacquin L, Geffroy P (2003) The mixing layer over a deep cavity at high-subsonic speed. J Fluid Mech 475:101–145

Freitas CJ, Street RL (1988) Non-linear transport phenomena in a complex recirculating flow: a numerical investigation. Int J Numer Methods Fluids 8:769–802

Gadoin E, Le Quéré P, Daube O (2001) A general methodology for investigating flow instability in complex geometries: application to natural convection in enclosures. Int J Numer Methods Fluids 37:175–208

Ghia U, Ghia KN, Shin CT (1982) High-Re solutions for incompressible flow using the Navier-Stokes equations and a multigrid method. J Comput Phys 48:387–411

Guermond JL, Migeon C, Pineau G, Quartapelle L (2002) Start-up flows in a three-dimensional rectangular driven cavity of aspect ratio 1:1:2 at Re = 1000. J Fluid Mech 450:169–199

Hirsch C (1987) Numerical computation of internal and external flows. Wiley, New York

Koseff JR, Street RL (1984a) Visualization studies of a shear driven three-dimensional recirculating flow. J Fluids Eng 106:21–29

Koseff JR, Street RL (1984b) On end wall effects in a lid-driven cavity flow. J Fluids Eng 106:385–389

Koseff JR, Street RL (1984c) The lid-driven cavity flow: a synthesis of qualitative and quantitative observations. J Fluids Eng 106:390–398

Leonard BP (1979) A stable and accurate convective modeling procedure based on quadratic upstream interpolation. Comput Methods Appl Mech Eng 19:59–98

Migeon C (2002) Details on the start-up development of the Taylor-Görtler-like vortices inside a square-section lid-driven cavity for 1,000 ≤ Re ≤ 3,200. Exp Fluids 33:594–602

Migeon C, Pineau G, Texier A (2003) Three-dimensionality development inside standard parallelepipedic lid-driven cavities at Re = 1000. J Fluids Struct 17:717–738

Navarro-Martinez S, Tutty OR (2005) Numerical simulation of Görtler vortices in hypersonic compression ramps. Comput Fluids 34:225–247

Pereira JCF, Sousa JMM (1995) Experimental and numerical investigation of flow oscillations in a rectangular cavity. J Fluids Eng 117:68–74

Saric WS (1994) Görtler vortices. Annu Rev Fluid Mech 26:379–409